Diamond & Related Materials 124 (2022) 108917

Contents lists available at ScienceDirect

Diamond & Related Materials

journal homepage: www.elsevier.com/locate/diamond

Microwave plasma modelling in clamshell chemical vapour deposition diamond reactors

Jerome A. Cuenca *, Soumen Mandal, Evan L.H. Thomas, Oliver A. Williams

School of Physics and Astronomy, Cardiff University, Cardiff, Wales, CF24 3AA, UK

ARTICLE INFO

Keywords:
Microwave plasma model
Cvd diamond
Finite element modelling

ABSTRACT

A microwave plasma model of a chemical vapour deposition (CVD) reactor is presented for understanding spatial heteroepitaxial growth of polycrystalline diamond on Si. This work is based on the $TM_{0(n>1)}$ clamshell style reactor (Seki Diamond/ASTEX SDS 6K, Carat CTS6U, ARDIS-100 style) whereby a simplified H_2 plasma model is used to show the radial variation in growth rate over small samples with different sample holders. The model uses several steps: an electromagnetic (EM) eigenfrequency solution, a frequency-transient EM/plasma fluid solution and a transient heat transfer solution at low and high microwave power densities. Experimental growths provide model validation with characterisation using Raman spectroscopy and scanning electron microscopy. This work demonstrates that shallow holders result in non-uniform diamond films, with a radial variation akin to the electron density, atomic H density and temperature distribution at the wafer surface. For the same process conditions, greater homogeneity is observed for taller holders, however, if the height is too extreme, the diamond quality reduces. From a modelling perspective, EM solutions are limited but useful for examining electric field focusing at the sample edges, resulting in accelerated diamond growth. For better accuracy, plasma fluid and heat transfer solutions are imperative for modelling spatial growth variation.

1. Introduction

Chemical vapour deposition (CVD) has become one of the most popular methods for epitaxial growth of single crystal diamond (SCD) and polycrystalline diamond (PCD) for a wide variety of applications. The basis of this technique requires dissociation of a gaseous carbon pre-cursor (CH_4) at low pressures using a reactive H_2 species that is excited either using hot filament (HFCVD) [1–7] or microwave plasma (MPCVD) [8–15]. Both HFCVD and MPCVD have their advantages and disadvantages for diamond growth. HFCVD offers easier scalability since the activation region simply depends upon the area covered by the tungsten or tantalum filaments. However, metal incorporation is possible [16,17], the filament stability is challenging [18] and growth rates are moderately low compared to other methods (~1.6 μm h^{-1}). MPCVD does not have filament issues since the plasma is formed using electromagnetic (EM) standing waves and the growth rates are much higher (>10 μm h^{-1}) [19], although only over small areas making scalability much harder. This makes MPCVD particularly useful for small, millimetre scale sample growth such as SCD for quantum applications [20,21].

The MPCVD diamond growth process can be broken into several steps: (1) evacuating the chamber to a base pressure, (2) introducing H_2 and maintaining a low pressure for plasma ignition, (3) microwave plasma ignition and formation of the plasma activation region, (4) introducing a small percentage of the CH_4 carbon pre-cursor and finally, (5) carefully increasing the power and pressure, otherwise known as the microwave power density (MWPD), until the sample temperature reaches ~800 °C. The plasma is typically focused into an ellipsoid above the sample where atomic H dissociates the CH_4, resulting in carbon deposition. Understanding the size and shape of the plasma activation region is therefore of huge importance as this directly influences the diamond deposition area.

The plasma region is affected by several process parameters including forward microwave power, pressure, gas flow rate and temperature in addition to physical parameters such as the sample size, sample holder geometry and of course the reactor topology. The effect of each may be understood empirically or through modelling approaches. Experimental data offers the greatest insight as no CVD reactor is the same as another, especially for bespoke builds. A notable example of this is shown for Asmussen et al. where for SCD, it has been empirically

* Corresponding author.
E-mail address: cuencaj@cardiff.ac.uk (J.A. Cuenca).

https://doi.org/10.1016/j.diamond.2022.108917
Received 22 November 2021; Received in revised form 25 January 2022; Accepted 8 February 2022
Available online 17 February 2022

shown that a recessed or 'pocket' type sample holder results in less unwanted PCD growth at the sample edges [22–24]. Significant material and machining costs are required in order to experimentally iterate geometrical adjustments. Modelling becomes extremely useful at this point and a viable approach for growth optimisation for various reactors, offering faster and cheaper insights into how modified stages, sample holders and reactor walls affect the plasma. Numerous reactor modelling studies exist to this end; the various transverse magnetic (TM) topologies include the cylindrical $TM_{01(p>1)}$ type cavity such as the ASTEX PDS-18, Seki Diamond SDS 5200 series reactors [25–29], the $TM_{0(n>1)}$ type cavity such as the ARDIS-100, Carat Systems CTS6U, Seki Diamond SDS 6K style clamshell [10,30–33], the TM_{02} dome style cavity as developed by Su et al. [34] and the ellipsoidal egg-shaped cavity such as the AIXTRON reactor [25,35,36]. For a comprehensive review of modelling different microwave reactor topologies, we referred to Silva et al. [37].

Plasma modelling is not trivial and requires significant development and experimental validation. Fortunately in this decade a number of commercial packages exist, making this avenue more accessible. One such area which requires more attention from the modelling perspective is the sample holder design. Shivkumar et al. have contributed significant understanding of pillar type models to focus the plasma, corroborated with optical emission spectroscopy [27]. A notably recent study by Sedov et al. combines both modelling and experimental growths of the geometrical effect of recessed and pedestal type sample holders for 2" Si wafers using an *E*-field model, demonstrating that pedestal holders yielded higher quality diamond films when compared to a recessed holder [38].

In this work, we demonstrate a simple microwave plasma model of the $TM_{0(n>1)}$ reactor (Seki Diamond 6K style) that can be implemented in COMSOL Multiphysics® for the purpose of sample holder or 'puck' design. The model presented here uses a simplified H_2 plasma model using a cross-section set currently accessible from the Itikawa database on lxcat.net [39]. A simple experimental validation is achieved using a sample puck of varying height, positioning the sample closer or further away from the plasma. The model is compared with experimental characterisation of thin film diamond growths over small Si wafers ($\varnothing = 1''$, $t = 0.5$ mm). In Section 2 the electromagnetic (EM) theory is briefly discussed for $TM_{0(n>1)}$ style reactors along with the plasma and heat transfer continuity equations for the finite element model (FEM). In Section 3 the modelling implementation is shown, including the boundary conditions and the modelling results. In Section 4 the experimental data is presented, including plasma images from the viewports, Raman spectra and scanning electron microscopy (SEM) images of the films.

2. Theory

2.1. Electromagnetic field

The microwave plasma is sustained by the electric (E) field which accelerates the seed electrons to interact with the H_2 gas molecules. The shape and location of the microwave plasma activation region is therefore dependent upon the spatial EM field distribution within the resonant chamber. One of the quickest methods of modelling the plasma location is to simply calculate the EM field distribution of the resonant mode through eigenfrequency analysis [28]. Analytically, these standing wave distributions are determined by deriving the Helmholtz resonator solution from the time-harmonic Maxwell's equations:

$$\nabla\cdot\mathbf{E} = \rho_c/\varepsilon_0 \tag{1}$$

$$\nabla\cdot\mathbf{B} = 0 \tag{2}$$

$$\nabla\times\mathbf{E} = -j\mu_0\mu_r\omega\mathbf{H} \tag{3}$$

$$\nabla\times\mathbf{H} = \mathbf{J} + j\varepsilon_0\varepsilon_r\omega\mathbf{E} \tag{4}$$

where $\mathbf{E}$ and $\mathbf{H}$ are the electric and magnetic fields, respectively, $\mathbf{J}$ is the current density, ε_r and μ_r are the relative permittivity and permeability of the medium, respectively, ρ_c is the charge density, ε_0 and μ_0 are the permittivity and permeability of vacuum, respectively, $\mathbf{B} = \mu_r\mu_0\mathbf{H}$ and ω is the angular frequency. A Helmholtz resonator solution is obtained using vector identities. For TM modes where $\mathbf{H}_z$=0 and $\mathbf{E}_z$ is finite:

$$\nabla^2\mathbf{E}_z - \omega^2\varepsilon_0\left(\varepsilon_r - j\frac{\sigma}{\varepsilon_0\omega}\right)\mathbf{E}_z = 0 \tag{5}$$

where σ is the conductivity of the medium. Analytical solutions can be derived based on the coordinate system, or solved for using FEM.

Microwave reactor topologies are typically cylindrical or elliptical since the standing wave patterns are based upon Bessel functions which inherently focus the *E*-field, and therefore the plasma, into the central regions of the cavity [28]. For example in cylindrical coordinates, $\nabla^2\mathbf{E}_z$ becomes a Poisson equation:

$$\frac{\partial^2\mathbf{E}_z}{\partial r^2} + \frac{1}{r}\frac{\partial\mathbf{E}_z}{\partial r} + \frac{1}{r^2}\frac{\partial^2\mathbf{E}_z}{\partial\theta^2} + \frac{\partial^2\mathbf{E}_z}{\partial z^2} - k^2\mathbf{E}_z = 0 \tag{6}$$

The radial component has solutions dependent on Bessel functions and the azimuthal and axial components have solutions based on sinusoidal functions. By imposing boundary conditions, the cylindrical TM $\mathbf{E}_z$ field can be obtained:

$$\mathbf{E}_z\left(r,\theta,z\right) = J_n\left(\frac{\alpha_{mn}}{a}r\right)cos(n\pi\theta)cos\left(\frac{p\pi}{l}z\right) \tag{7}$$

where J_n is the n^{th} order Bessel function a and l are the radius and height of the cylinder, respectively, α_{mn} is the n^{th} root of the m^{th} Bessel function and p is the integer number of axial standing waves. One can then derive all other components of the field distribution using (1) to (4), however, from this equation it is clear which TM modes will be useful for an MPCVD reactor. From a practical point of view, the substrate should be placed in the centre of the reactor as to be as far from the walls as possible to avoid any etch or re-deposition of wall contaminants. Firstly, this means that $p>0$ otherwise the absence of an axial standing wave would directly connect the plasma to the top and bottom of the cylindrical cavity walls. Secondly, in order to achieve a centralised plasma, only TM modes which consider *E*-fields where m=0 can be used as this is the only Bessel function where the result is non-zero and finite at r=0. It has been shown that modes where $m>0$ can actually be used to monitor the temperature of a cavity resonator as they are less sensitive to the centre [40,41]. Bessel functions roughly decay proportional to $r^{-1/2}$ and with increasing root and frequency, the E-field is further compressed and concentrated into the centre of the cavity. Thus, the ideal case is to use the highest n possible although this would make a cavity with a very large radius. This defines the conventional use of cylindrical reactors based on $TM_{0(n>1,p>1)}$ modes as it places the *E*-field central and at either the top or bottom of the cavity. A sample holder becomes crucial to break this degeneracy by disrupting the E-field and encourages the plasma to be localised to only one of these regions.

While the E-field distribution provides a general idea as to where the plasma is to be localised, the simple EM field eigenfrequency approximation does not take into account the perturbation of the diffuse but conductive gas. In this case, the conductivity of the gas is complex and can be approximated using the Drude-Lorentz model:

$$\sigma = \frac{n_e e^2}{m_e(\nu_m + j\omega)} = \frac{\varepsilon_0\omega_p^2}{(\nu_m + j\omega)} \tag{8}$$

where ω_p is the plasma frequency, ν_m is the electron-species collision frequency, n_e is the electron density and e and m_e are the electron charge and mass, respectively. The power that is then dissipated into the gas is then simply:

$$Q_{\mathrm{mw}} = \frac{1}{2}\Re(\mathbf{J}\cdot\mathbf{E}^{*}) \tag{9}$$

where Q_{mw} is the microwave Joules heating of the electrons and $\mathbf{E}^*$ is the complex conjugate of the $\mathbf{E}$ field. To introduce the gas of a certain electron density, the microwave frequency and information on how frequently the electrons interact with the pre-cursor gas is needed. Notable methods to incorporate this are the early Füner models, where at a defined threshold E-field value, n_e would be finite and zero otherwise [25,27,42]. While this method is suitable at high pressure such that the plasma ball is confined within the E-field region, this never allows the plasma to be situated in the nodal regions of the standing wave, which contradict the large pancake plasma shapes typically found in $\mathrm{TM}_{0(n>1)}$ style reactors at low pressures.

2.2. Plasma fluid

To fully incorporate the nuance of pressure in larger area reactors, the fluid model is introduced which allows modelling of the collective behaviour of the electrons, ions and neutral species [29,43–45]. These gaseous species are initially distributed homogeneously within the cavity and several energy dependent electron-impact reactions are defined with a rate constant or reaction cross section. An example of a simplified reaction set is shown in Fig. 1. The accelerated electrons may result in a number of reactions including but not limited to elastic scattering ($e + H_2 \rightarrow e + H_2$), excitation of a species, ($e + H_2 \rightarrow e + H_2^*$), ionisation ($e + H_2 \rightarrow e + H_2^+$) or attachment/detachment of atoms ($e + H_2 \rightarrow e + 2H$). Additional reactions can also occur with these products, creating a soup of various charged and neutral species. As electrons and ions are produced, electrostatic forces and concentration gradients then result in a plasma fluid diffusing around the high E-field regions. The key advantage of the fluid approach is that the plasma has a finite density, allowing the fluid to be modelled as a function of pressure, temperature and even the gas flow velocity.

For the electrons, the fluid is modelled using continuity equations of

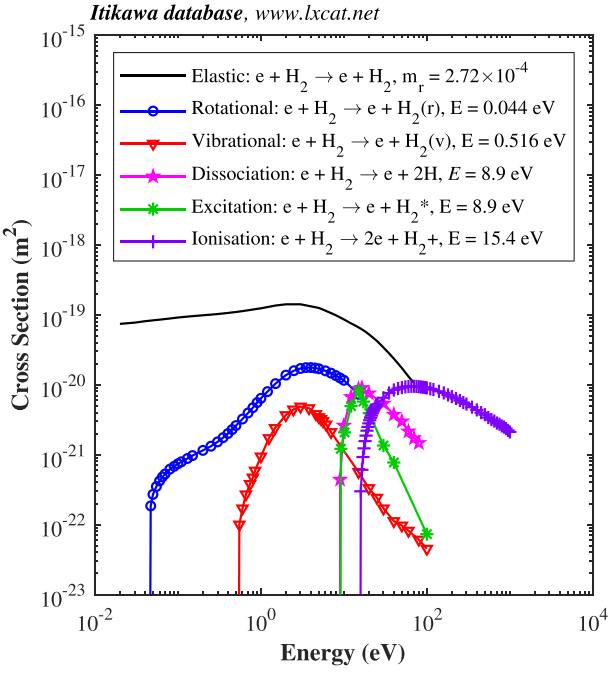

Fig. 1. Simplified electron impact cross section with H_2 from the Itikawa [39] database (www.lxcat.net, retrieved on September 3rd, 2021). The chosen electron impact reactions are the elastic/momentum exchange (solid), rotational excitation H_2 (J=0→2) ('o'), vibrational excitation H_2 (v=0→1) ('▽'), $b^3\Sigma_u^+$ excitation and H_2 dissociation to 2H ('☆','*') and ionisation to H_2^+ ('+').

motion and energy conservation equations. The equation of motion for the number density is:

$$\frac{\partial n_e}{\partial t} + \nabla\cdot\Gamma_e = R_e \tag{10}$$

$$\Gamma_e = -\mu_e n_e \mathbf{E}_a - \nabla D_e n_e \tag{11}$$

where n_e is the electron density, Γ_e is the electron flux vector, μ_e is the electron moblity, D_e is the electron diffusivity, $\mathbf{E}_a$ is the ambipolar field and R_e represents the electrons that are either produced or consumed during impact reactions. The first term in the RHS of (11) is associated with the ambipolar E-field and is the E-field that is generated by the separation of the ions and the electrons. The second term is associated with drift contributions from concentration gradients. Coupled with (10) is an electron energy conservation equation of a similar form. Energy is either lost or gained from elastic/inelastic reactions with the gaseous species, absorbed from microwave heating in the E-field or accelerated in the electrostatic ambipolar fields:

$$\frac{\partial n_\varepsilon}{\partial t} + \nabla\cdot\Gamma_\varepsilon + \mathbf{E}_a\cdot\Gamma_e = S_\varepsilon + \frac{Q_{\mathrm{mw}}}{e} \tag{12}$$

$$\Gamma_\varepsilon = -\mu_\varepsilon n_\varepsilon \mathbf{E}_a - \nabla D_\varepsilon n_\varepsilon \tag{13}$$

where n_ε is the electron energy density, Γ_ε is the electron energy flux vector, μ_ε is the electron energy mobilty, D_ε is the electron energy diffusivity, S_ε is the energy gain or loss from impact reactions.

The net electrons that are produced or consumed (R_e) and the net energy gain or loss (S_ε) terms are defined by:

$$R_e = \sum_{i=1}^{M} x_i k_i N_n n_e \tag{14}$$

$$S_\varepsilon = \sum_{i=1}^{P} x_i k_i N_n n_e E_i \tag{15}$$

where x_i, k_i and E_i are the mole fraction of the specie, the rate coefficient and energy loss of the i^{th} reaction, respectively and N_n is the neutral number density. The rate coefficients are dependent upon the cross-section data (eg. those in Fig. 1) and a Maxwellian electron energy distribution function (EEDF):

$$k_i = \sqrt{\frac{2e}{m_e}}\int_0^\infty \varepsilon\sigma_k(\varepsilon)f(\varepsilon)d\varepsilon \tag{16}$$

where ε is the electron energy, f is the EEDF and σ_k is the reaction cross-section. The reaction rates are then used to calculate the electron-species collision frequency which feeds into the plasma conductivity in (8). The electron temperature for the Maxwellian EEDF is defined as:

$$T_e = \frac{2}{3}\bar{\varepsilon} \tag{17}$$

where $\bar{\varepsilon}$ is the mean electron energy.

For the heavier gas species such as ions and neutral molecules, the continuity equations are similar to the electrons, however, may include inertial terms from the background gas flow velocity (omitted in this model). For multiple reaction species (H, H_2, H_2^+ and H_2^*), the continuity relation for the i^{th} specie is:

$$\rho_i\frac{\partial w_i}{\partial t} = \nabla\cdot\Gamma_i + R_i \tag{18}$$

$$\Gamma_i = \rho_i w_i v_d \tag{19}$$

where ρ_i is the density, w_i is the mass fraction, Γ_i is the ion flux vector, R_i represents the ions that are either produced or consumed in reactions and v_d is the species diffusion velocity.

2.3. Heat transfer model

In addition to the plasma fluid model, the gas temperature (or heavy species temperature) is calculated separately assuming a simple conductive heat transfer model using a gas density, heat capacity and thermal conductivity from a COMSOL Multiphysics® defined hydrogen material for glow discharges and the EM power dissipated in the plasma model. The continuity equations for this calculation are:

$$\rho C_p \frac{\partial T}{\partial t} = \nabla \cdot \left(k \nabla T \right) + Q_{\mathrm{mw}} \tag{20}$$

where ρ is the gas density, T is the temperature, C_p is the heat capacity and k is the thermal conductivity. The walls of the reactor are assumed to be cooled to stop thermal runaway of the plasma. The cooling fluxes are defined as:

$$q_0 = h_c (T_{\mathrm{ext}} - T) \tag{21}$$

where q_0 is the heat flux, T_{ext} is the external temperature and h_c is the heat transfer coefficient that models the cooling power.

3. Modelling

3.1. Method

The FEM process is split into three separate studies as shown in Fig. 2. First, the EM model is run where the eigenfrequencies of the geometry are calculated to ensure that the correct mode is identified (the $TM_{0(n>1)}$ type mode where a TM_{011} distribution is present in the active region of the reactor). This step is crucial for determining if any reactor modifications or the introduced sample holders shift the frequency away from the source generator frequency range. Additionally, higher order modes which are not necessary for diamond growth can also be identified. Secondly, the frequency-transient EM/plasma model is calculated at the eigenfrequency. The reactor port power is varied and provides a continuous wave to set up the EM standing wave. In this way the E-field intensity, and therefore the plasma, is power dependent. The electrons and gaseous species are distributed within the cavity and the transient response is modelled from 0 to 10 s to allow the plasma fluid to evolve to a steady state at an initial power and pressure (1.5 kW at 27 mbar) or low MWPD. Subsequently, the MWPD is ramped up to growth conditions or high MWPD (5 kW at 160 mbar) over the simulated time of 1 h to keep the solution stable. Finally, the third step calculates a heat transfer solution to obtain the gas temperature using the microwave power dissipated in the plasma.

The cavity boundary conditions are shown in Fig. 3. The mesh is kept consistent in all steps, utilising a free triangular mesh with boundary layers at the extremities for the plasma solution. The mesh also forces a distribution of 50 nodes across the Si sample surface to ensure a high resolution for the spatially dependent electron and species densities. For

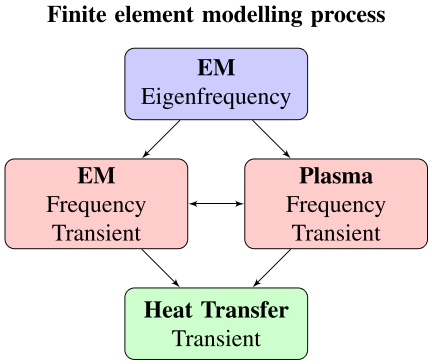

Fig. 2. Finite element modelling process flow using COMSOL Multiphysics®.

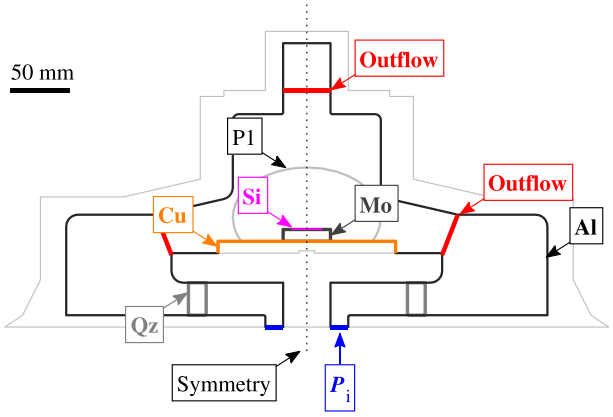

Fig. 3. Simplified schematic of the clamshell reactor (Carat Systems CTS6U). Wall surfaces are modelled as impedance boundary conditions. The dotted line denotes axial symmetry about r=0. P_i denotes a lumped coaxial port boundary condition. The red outflow lines denote the limits of the fluid simulation as electron and heat outlets for the plasma and heat transfer solutions, respectively. P1 denotes the location of the plasma region. (For interpretation of the references to colour in this figure legend, the reader is referred to the web version of this article.)

the first EM eigenfrequency model, the chamber domain is assumed vacuum and the walls are all modelled as metallic impedance boundary conditions (σ>10^7 S/m).

For the plasma model, only the domain in the centre of the reactor is used to reduce the computation time, marked by the outflow/electron outlet conditions in Fig. 3. All other surfaces are defined as wall boundary conditions. The gas pressure of this domain is varied from 27 to 160 mbar. All walls are defined as grounds with additional surface reactions for excited species to relax to neutral species (eg. $H_2^* \rightarrow H_2$, $H_2^+ \rightarrow H_2$ and $H + H \rightarrow H_2$). The reactor port P_i is defined as a lumped port with excitation varying from 1.5 to 5 kW. To minimise the computational time, the simplified reactions for the H_2 gas are those plotted in Fig. 1. It is worth noting that the H_2^+ ionisation reaction is assumed to form into H_3^+ as it is well-known to be the dominant species (eg. $H_2^+ + H_2 \rightarrow H_3^+ + H$) [46]. The elastic/momentum transfer data is potentially unresolved with vibrational contributions (quoted as the 'vibrationally elastic' cross-section [39]). Since the rotational/vibrational states are typically short lived [30] the models were calculated assuming these contributions to be lumped into the elastic/momentum transfer cross section. Thus, all H_2 species is considered to be already in an equilibrium vibrationally excited state. The absence of these cross-sections made minimal difference to the computed H_2, H and electron number densities and distributions, and resulted in a much more stable model compared to their inclusion. Results presented herein therefore assume the rotational and vibrational contributions to be in the elastic/momentum transfer cross-section. For the heat transfer model, the domains are the same as those for the plasma model with the addition of the Si and the Mo as solids. Heat flux boundary conditions are imposed to all of the walls to prevent the solution from thermal runaway. All heat flux boundaries used a fixed systematic heat transfer coefficient for all models (h_c= 1700 W m^{-1} K for external boundaries and 770 W m^{-1} K underneath the Mo puck with T_{ext}= 25 °C). The sample is modelled as a Si wafer (⌀=1″, t= 0.5 mm) and is positioned on top of the Mo sample holder puck ($\varnothing_{\mathrm{puck}}$=40 to 60 mm, h_{puck}= 1 to 20 mm). The corners of the sample are rounded with a radius of 0.1 mm and the Mo holder rounded with a radius of 0.2 mm to ensure a high mesh density at the anticipated high E-field regions and avoid convergence errors.

3.2. Electromagnetic model

Fig. 4 shows the EM eigenfrequency model with the E-field

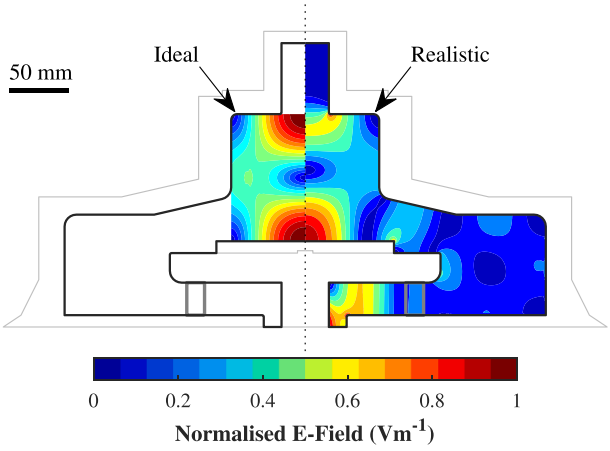

Fig. 4. The base EM eigenfrequency model without the Mo sample holder puck. The *E*-field is normalised to the maximum value. For comparison and identification of the correct mode, the ideal cylindrical case of the TM_{011} mode (left side) and the realistic $TM_{0(n>1)}$ design (right side) are shown.

distribution of an ideal TM_{011} mode and the $TM_{0(n>1)}$ reactor without the Mo sample puck. The $TM_{0(n>1)}$ reactor mode shows a reasonably similar E-field distribution to the ideal case, demonstrating that the correct mode has been identified. In this mode, there is an E-field node separating the central region and a side lobe. High intensity E-field regions at the edge of the stage are found where a secondary plasma can also be sustained. Fig. 5 shows how the calculated resonant frequency of the EM model is perturbed to lower frequencies as a Mo sample puck is introduced. With the current dimensions, the initial unperturbed resonant frequency is calculated at approximately 2.45 GHz. The results show that wider pucks have less of a frequency shift, while taller pucks alter the resonant frequency by as much as $\Delta f \approx$ -66 MHz at h_{puck} = 20 mm. This demonstrates that shorter sample pucks are more favourable for stable operation with a magnetron with a fixed frequency output. Interestingly, this is not so much a problem for solid state sources since the generator frequency can be varied.

After introducing the puck, the *E*-field distribution of the EM model is shown in Fig. 6 (a). The E-field is perturbed and high intensity regions occur at the corners of the puck. This is simply because of Eqs. (1) and (7); the E_z field lines should be perpendicular to the Cu stage and the introduction of a metal object creates parallel surfaces that disrupts this condition resulting in a reconfiguration of surface currents. With increasing sample holder puck height, the E-field, and therefore the

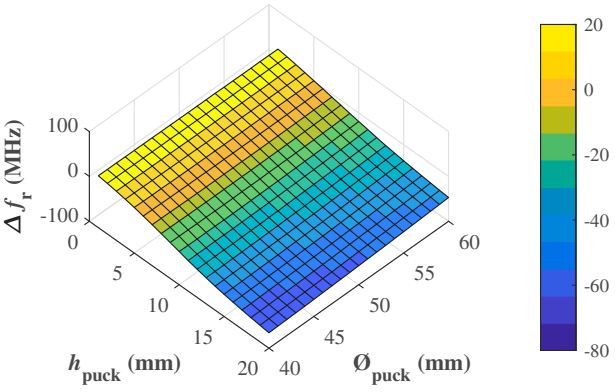

Fig. 5. Modelled shift in resonant frequency caused by the Mo sample holder puck of varying dimensions; h_{puck} and $\varnothing_{puck}$ denote the height and diameter, respectively. The holder has a Si wafer sample on top ($\varnothing$= 1″, *t*= 0.5 mm).

plasma activation region, is concentrated towards the edges of the holder. The nodal regions of the E-field are also clearly visible either side of the puck where, based on the threshold modelling approach, the plasma could not exist; or if it did, the plasma could exist in multiple regions in the cavity. It is also noted that with increasing sample holder height, the E-field hot spots at the top of the chamber reduce in intensity, decreasing the likelihood for a secondary plasma to ignite at these regions.

3.3. Plasma model

The plasma fluid models are shown in Fig. 6 (b) to (e) and clearly demonstrate a focused electron and atomic H density in the sample region. The calculated electron densities are as high as 2.4×10^{17} m^{-3} and 12×10^{17} m^{-3} in the low and high MWPD models, respectively. Based on a ω_p= 2.45 GHz, n_e=7.45 $\times$ 10^{16} m^{-3}, stipulating that at these electron densities, the microwaves are not able to propagate freely through the plasma and thus attenuates, thereby depositing microwave power into the plasma [37]. Note that in the low MWPD solution both the electron and atomic H density distributions are much wider than the E-field result, demonstrating that simple EM solutions are potentially less appropriate for modelling low pressure microwave plasmas. Although PCD diamond growth with low non-diamond carbon impurities typically occurs at high MWPD, the lower pressure solutions are an imperative result for several purposes. The first is that some applications involve nano-crystalline diamond (NCD) and ultra-nanocrystalline diamond (UNCD) growth which is typically at low MWPD [47–49] as well as hybrid graphene-diamond films [50]. The second is to ensure that the plasma can actually be ignited at the right place in the chamber. Finally, investigating large area growth using lower pressure would be challenging using an EM solution alone. At low MWPD and at large heights of 15 to 20 mm, the sample is pushed further into the the plasma and the fluid moves towards the outlets at the side of the stage. This is not favourable as the risk of the plasma pushing to below the stage towards the quartz ring region where the microwaves enter is much greater. At high MWPD, the plasma becomes the familiar elliptical shape situated over the sample with a smaller area and a much higher electron/H density, similar densities to those found in previous models of different reactors at growth conditions [44,45,51]. At high MWPD, higher Mo sample pucks result in the plasma further focusing towards the edges which will inherently affect the spatial CVD diamond growth across the sample.

3.4. Temperature and heat transfer model

The electron temperatures at low and high MWPD are shown in Fig. 7 (a) and (c). The electron temperatures in the plasma region range from approximately 1 to 1.6 eV in the low MWPD solution with a wide spatial distribution across the sample surface. Maximum values are observed at the edges of the sample holder. As the sample holder height is increased, there is minimal change in the electron temperature in the vicinity of the sample substrate. At high MWPD, the electron temperature distribution is similar to that of the *E*-field distribution in the eigenfrequency solution.

The gas temperatures for the heat transfer solutions are shown in Fig. 7 (b) and (d). For the low MWPD solution the gas temperature reaches as high as 1800 K in the centre of the plasma while at high MWPD, the centre reaches approximately 3000 K. At shallower puck heights, the gas temperature is hotter and decreases significantly as the puck is pushed into the plasma. This is likely due to the fact that the sample puck is in direct contact with the heavily cooled Cu stage underneath and an increasing volume of Mo increases the contact with the plasma, thereby cooling it. The electron and gas temperatures found here are similar to those reported by several authors previously at similar growth conditions [30,32,34,52]. The significantly higher electron temperatures compared to that of the gas demonstrates thermal

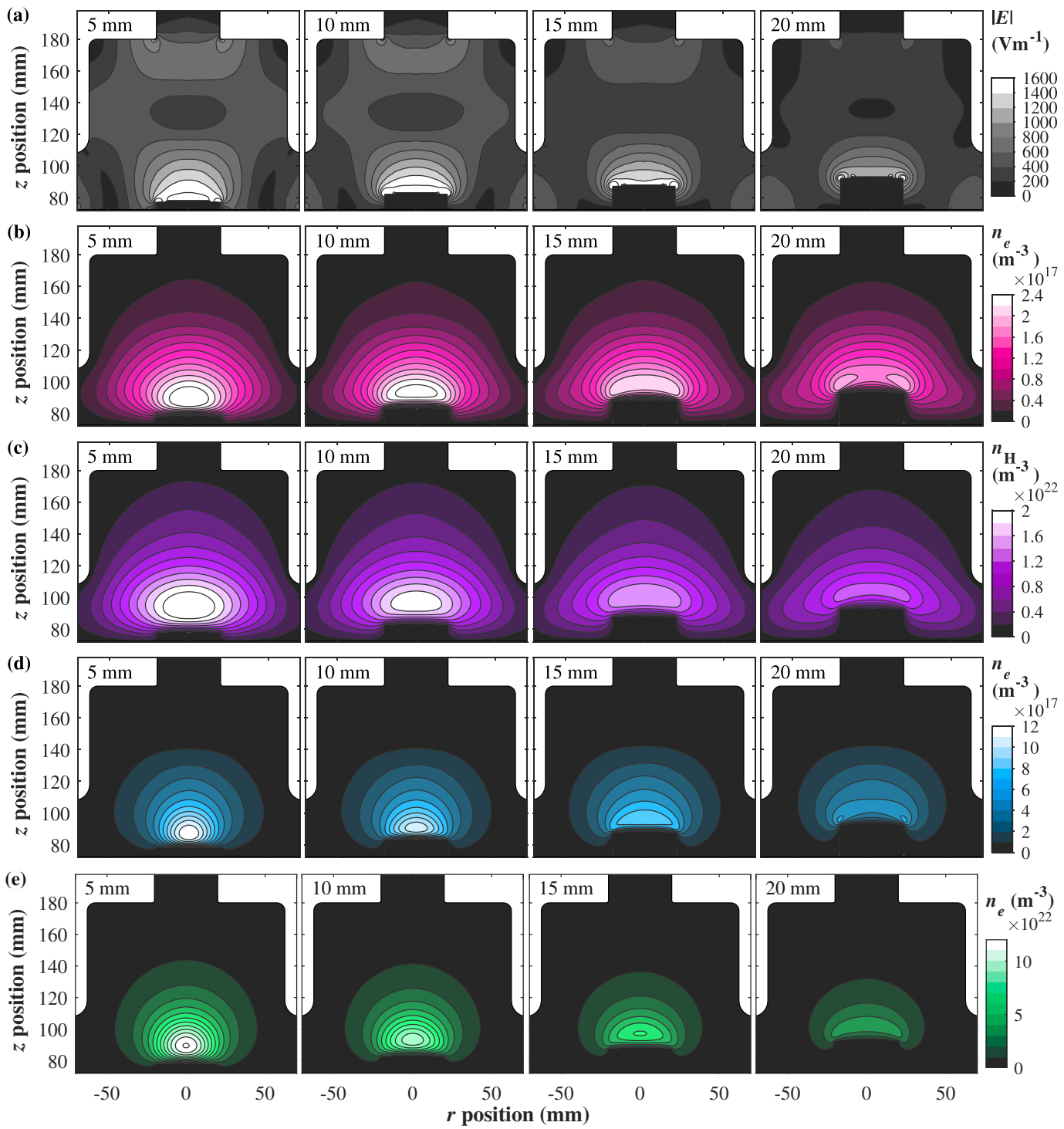

Fig. 6. Microwave H_2 plasma model using the eigenfrequency, plasma coupled and heat transfer solution method for varying sample holder heights (h_{puck} = 5 to 20 mm) with a Si wafer on top (⌀= 1″, t= 0.5 mm). Model shows the (a) eigenfrequency electric field (2.4 to 2.5 GHz), (b) electron number density and (c) atomic H number density at low MWPD (1.5 kW, 27 mbar) and (d) electron number density and (e) atomic H number density at high MWPD (5 kW, 160 mbar).

non-equilibrium at these conditions in this reactor.

4. Experiment

4.1. Experimental method

To demonstrate the overall affect of the sample holder height on the CVD diamond process, three Mo pucks were machined (⌀= 40 mm, h_{puck}= 5, 10 and 15 mm) and used for thin film growths (approximately 1 μm thick) on small Si wafers (⌀= 1″, t= 0.5 mm). It is worth stipulating that a fourth puck (h_{puck}=20 mm) was also machined, however, stable plasma ignition was not possible. This is likely due to the holder significantly perturbing the resonant frequency of the chamber. The Si wafers were seeded using the ultrasonic seeding process [53,54]. Briefly, the wafers were solvent cleaned and placed in a nanodiamond colloidal solution with particles of a positive zeta potential whilst under ultrasonic agitation for 10 min. The samples were then rinsed in deionised water, dried using an air gun and placed on the top of the sample holder

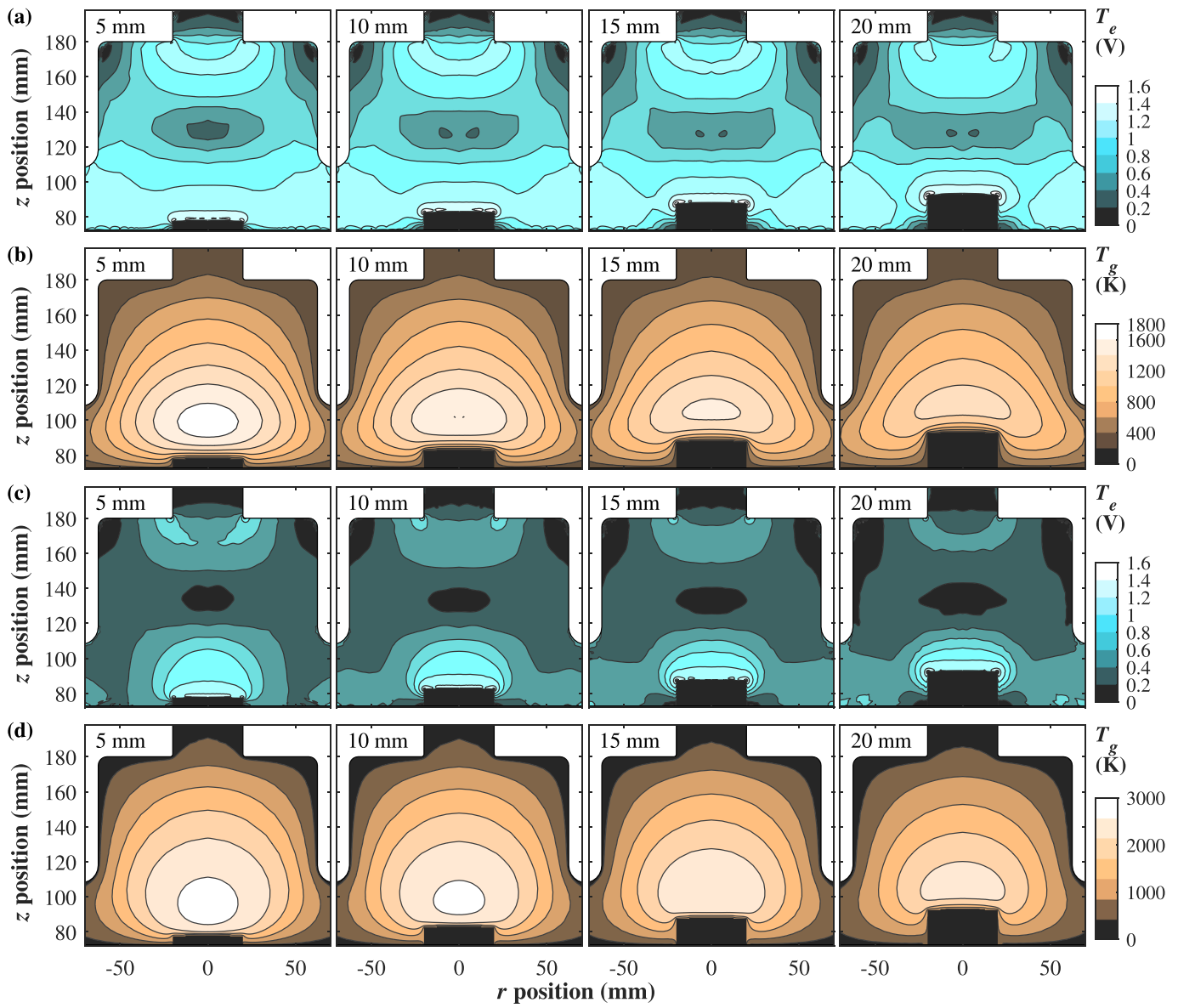

Fig. 7. Temperature distributions of microwave H_2 plasma model using the plasma coupled and heat transfer solution approach for varying sample holder heights (h_{puck} = 5 to 20 mm) with a Si wafer on top (⌀= 1″, t= 0.5 mm). Model shows the (a) electron temperature and (b) gas temperature at low MWPD (1.5 kW, 27 mbar) and (c) electron temperature and (d) gas temperature at high MWPD (5 kW, 160 mbar).

inside of a $TM_{0(n>1)}$ style reactor for CVD diamond growth. Samples were grown using a CH_4 / H_2 gas mixture with a CH_4 concentration of 3% in a total flow rate of 300 sccm at a forward microwave power of 5 kW at 160 mbar. The total growth time for all samples was fixed at 30 min, followed by a 5 min cool down ramp to 1.5 kW at 27 mbar. The temperature at growth MWPD was monitored using a Williamson dual wavelength pyrometer (DWF-24-36C), giving initial measured readings of approximately 760, 790 and 770 °C for the 5, 10 and 15 mm growths, respectively. Two samples for each Mo puck height were grown at different reactor usage times.

After growth, the samples were examined using Raman spectroscopy and scanning electron microscopy (SEM). Raman spectroscopy was conducted using a Horiba LabRAM HR Evolution with a green laser (λ= 532 mm) and a grating of 600 l mm^{-1} from 200 to 2000 cm^{-1} to allow for sensitivity to both the diamond and non-diamond carbon content. Line scans were taken at points across the samples (N = 20 points over 22 mm). SEM images were obtained using a Hitachi SU8200 (10 kV at 10 μA) with a working distance of 8 mm.

4.2. Microwave plasma

Fig. 8 shows the typical images of a microwave H_2 / CH_4 plasma just after ignition and at the point of reaching diamond growth conditions with different puck heights in the $TM_{0(n>1)}$ reactor. At low power density the plasma emits a purple glow associated with the combined emissions of the H_α (~657 nm), H_β (~486 nm) and the H_γ (~437 nm) lines [55]. As the MWPD is increased, the plasma becomes the familiar green ellipsoid over the sample holder with characteristic of C_2 emission from the low CH_4 concentration. The images show that the low pressure plasma extends well beyond the extents of the puck, into where the EM E-Field nodes are calculated to be. The edges of the 15 mm puck are also much brighter compared to the 5 mm puck owing to the E-field focusing. The increase in MWPD results in a smaller and focused ellipsoid above the puck, with the higher 15 mm puck distorting the bottom edges of the plasma ellipsoid.

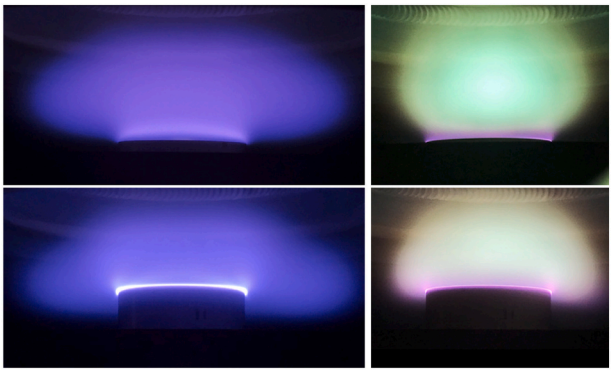

Fig. 8. Photographs of the microwave H_2 / CH_4 plasma at low (left column) and high (right column) MWPD for sample puck heights of 5 mm (top row) and 15 mm (bottom row), respectively. Low MWPD plasma is at 1.5 kW at 27 mbar, while high MWPD is 5 kW at 160 mbar with 3% CH_4 in a total flow rate of 300 sccm. Images were taken from the side viewport of the Carat Systems CTS6U using an Apple iPhone 7.

4.3. Scanning Electron microscopy

SEM images of the films are shown in Fig. 9 at incremental regions from the centre towards the edge of the 1″ Si wafer. These images show clear radial variations in growth rate depending on the height of the sample puck. Starting with the film grown at a height of 5 mm, at a radial position of 0 mm (centre of the film) shows a large size distribution with grains as large as ~1 μm down to the nanoscale. At 2.5 mm, these large micron size grains are still apparent, however are fewer in distribution and a larger fraction of nanoscale grains is found. Moving further outwards, the micron size grains begin to disappear, and only nanoscale grain texturing is observed. Finally reaching the edges of the film, the grain size suddenly increases showing significant growth of a microcrystalline film. Next, for the film grown at a height of 10 mm, there is minimal radial grain size variation from 0 up to 10 mm, showing similarly large micron size grains as the 5 mm sample except has coalesced with less nanoscale grains. However, at the edge of the film there is a clear jump again in growth rate with evidence of much larger grains. Finally, for the film grown at a height of 15 mm, the centre of the film also shows minimal radial variation from 0 up to 10 mm with the exception of a much smaller average grain size. In a similar fashion to the previous samples, the growth rate towards the edges of the film is much faster and much larger grains are found.

4.4. Raman spectroscopy

Raman spectra at the centre of the wafers of the thin diamond films grown at different Mo puck heights are shown in Fig. 10 (a). The high intensity peak at 520 cm^{-1} and the band at approximately 950 cm^{-1} are attributed to the first and second order bands of Si [14,56]. Since the growth time is fairly short, the diamond films are fairly thin, therefore the contribution of the Si substrate is large. The sharp peak at 1332 cm^{-1} is attributed to the first order sp^3 carbon peak, a signature characteristic of diamond [56–60]. Amongst this diamond peak are several broad bands associated with various non-diamond carbon impurities. The weak band at approximately 1420 cm^{-1} and even weaker band at approximately 1120 cm^{-1} are both attributed to *trans*-polyacetylene (tPA), commonly found in CVD diamond Raman spectra although are only dominant at particularly low grain sizes such as nanocrystalline diamond (NCD) [49,61,62]. The broad band at approximately 1310 to 1340 cm^{-1} is attributed to the breathing mode of aromatic sp^2 carbon rings, while the peak at around 1580 to 1610 cm^{-1} is attributed to the bond stretching mode in sp^2 carbon [62]. The low intensity of these bands compared to the sp^3 peak at an excitation wavelength of 532 nm implies a low non-diamond carbon impurity content; in heavily sp^2 incorporated films, these bands often dominate the sp^3 peak [47,53].

The line scans of the d / G ratio, or implied sp^3 / sp^2 ratio, in Fig. 10 (b) show that there is a significant variation in the diamond growth quality across the 1″ Si wafer. For all samples, the sp^3 / sp^2 peak ratio is much higher at the edges of the sample compared to the centre. This implies that non-diamond carbon is being etched at a greater rate at the edges of the sample. At a radial position of approximately 10 mm from the centre, the sp^3 / sp^2 peak ratio increases rapidly for all sample heights. For the film grown at a height of 5 mm, almost no diamond peak is found whereas for the films grown at heights of 10 and 15 mm, the sp^3

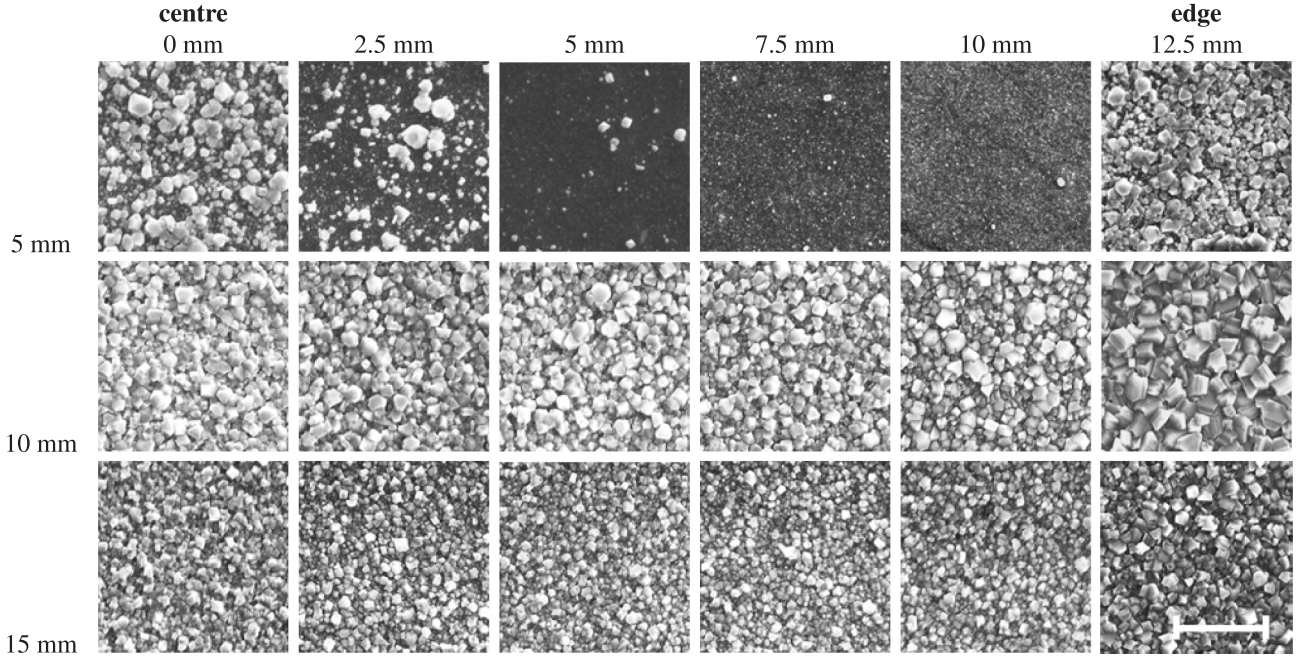

Fig. 9. SEM images of the CVD diamond films grown at varying Mo sample holder heights (5, 10 and 15 mm). Images are taken at fixed radial distances from the centre of the wafer to the edge. Scale bar represents a 5 μm length.

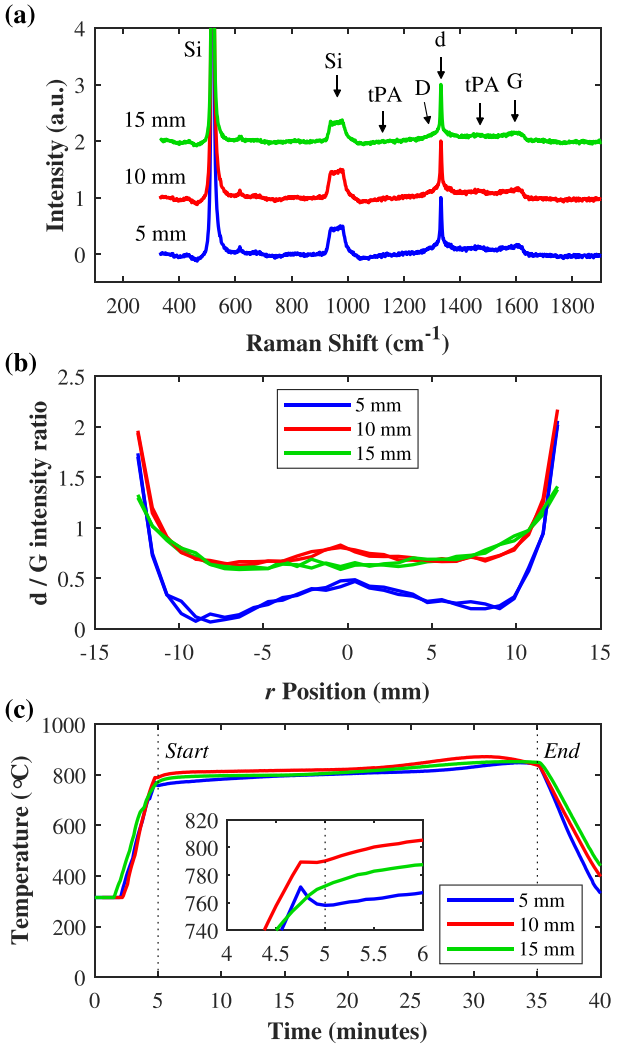

Fig. 10. Raman spectroscopy of CVD diamond on 1″ Si wafers grown at holder heights of 5 mm, 10 mm and 15 mm for 30 min (5 kW 160 mbar). (a) shows the spectra at the centre of the wafer. The labels 'd', 'D', 'G' and 'tPA' denote the contributions from the sp^3 carbon peak in diamond, the D and G bands of sp^2 carbon and *trans*-polyacetylene, respectively. (b) shows a line scan of the intensity ratio of 'd' / 'G', or the implied sp^3 / sp^2 or non-diamond carbon ratio. (c) shows the temperature recorded by the pyrometer, where the inset shows a zoom in at the start point. Pyrometer lower limit is 315 °C.

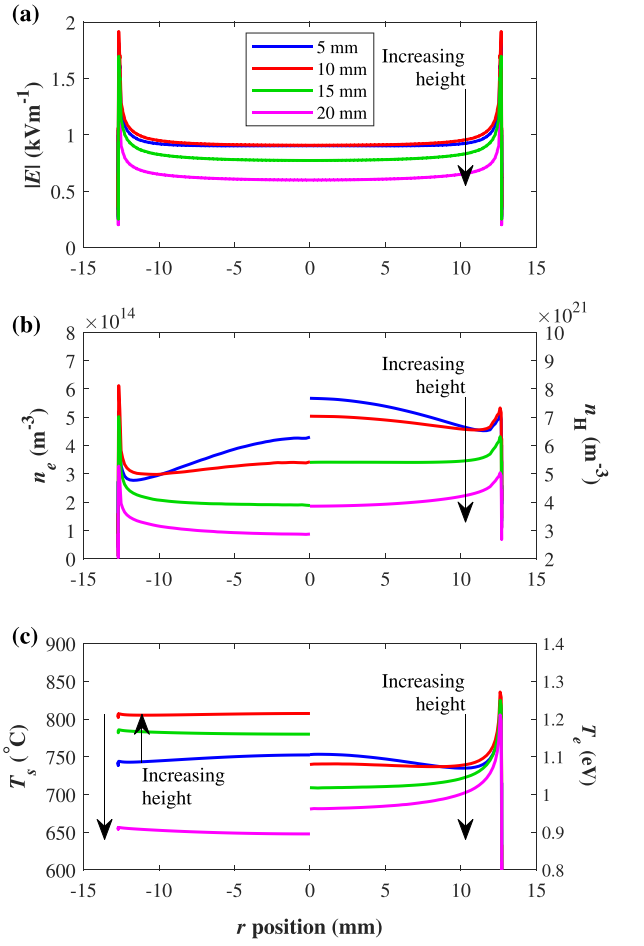

Fig. 11. Model line scans over the Si sample surface of (a) the *E*-field magnitude in the EM model, (b) the plasma electron number density (left) and the atomic H number density (right) and (c) the substrate temperature (left) and electron temperature (right).

/ sp^2 ratio is fairly similar towards the centre of the film. At the centre, a noticeable hump in the sp^3 / sp^2 ratio is found, which gradually disappears with increasing puck height.

5. Discussion

It is clear from the modelling and experimental results that the Mo sample puck height has a considerable effect on the plasma shape and therefore the spatial diamond growth quality and rate across a 1″ Si wafer. For comparison between the model and the experiment, Fig. 11 shows line scans of the E-field magnitude, plasma electron density, atomic H density, electron temperatures and substrate temperatures across the sample from the EM, plasma and heat transfer solutions. Clear correlations and limitations in the model are identified when compared with the SEM and Raman data.

For the EM model, the E-field distribution only shows the high intensity regions at the edges of the sample and almost no sign of the broad hump in the centre where the diamond is expected to grow (as verified by the SEM and Raman data). This highlights a limitation of the E-field modelling approach in predicting growth variations across small samples.

For the plasma model, electron/atomic H densities in Fig. 11 (b) also show the high intensity regions at the edges, however, clearly shows the bump at the centre of the film which becomes increasingly flatter as the puck height is increased. The electron/atomic H densities give a far better indication of the growth quality variations. The radial variation in the Raman sp^3 / sp^2 peak ratio is very likely to be due to the fact that atomic H preferentially etches non-diamond carbon and contributes to the critical surface hydrogen abstraction and re-termination process that allows diamond to grow [63]. Thus, diamond film quality can in some ways be inferred from the electron/atomic H density. Additionally, the spatial growth rate variations observed by SEM per sample can also be explained by the atomic H density, since it is responsible for generation of CH_3 diamond growth species (eg. $H + CH_4 \rightarrow CH_3 + H_2$). However, since this model does not explicitly calculate the CH_3 species distribution (or other species for that matter), this is only inferred and more complex multiple gas phase models are required. It is well-known that in MPCVD processes, CH_3 species tend to be situated at the periphery of a H_2 plasma at high pressures and low sample heights as has been demonstrated by Mankelvich et al. [64,65] and for clamshell reactors, Yamada et al. [30,66]. This is indeed a plausible reason for the increased growth rate at the edges, but less of an argument for the centre.

Relying on the values of the electron/atomic H density alone in the presented model implies that the growth rate would be much faster for a shallower puck over a taller puck which does not appear to not be the

case from the SEM images; at the centre of the sample grown at a height 5 mm, the film has yet to fully coalesce, however the film at 10 mm has coalesced. The reason is likely due to the temperature at the sample surface during growth. The experimentally measured temperature is shown in Fig. 10 (c) where the temperature is lower for the 5 mm puck (~760 °C) when compared to the 10 mm (~790 °C) and 15 mm (~770 °C) pucks. Thus, the plasma model is only representative of some spatial growth variation but less accurate when used to compare between holders. The heat transfer solution provides a slightly better insight as is shown in Fig. 11, where the temperature line scans show both the radial variation in temperature and that the 10 mm puck has a higher growth temperature than the others, thereby producing a film with larger grains overall.

The result from this experiment is that shallower pucks are heavily cooled by the stage which reduces the substrate temperature for a given process growth condition. As the height of the puck increases, the sample is pushed into the plasma and the substrate temperature increases. However, if the puck is too tall, the plasma is largely perturbed and then focuses to the edges and away from the sample substrate. Additionally, since a larger volume of Mo is in contact with the cooled stage, the T_g is reduced and therefore the substrate temperature. This model demonstrates that if the users goal is to optimise spatial homogeneity across a sample then this puts precedence on monitoring the spatial temperature across the sample during growth.

6. Conclusion

Modelling of microwave hydrogen plasmas can offer simple and cost effective insights into how sample holder designs can affect MPCVD processes. This work demonstrates that EM eigenfrequency models show how sample holder pucks of different width and diameter can perturb the reactor frequency where in this instance, taller pucks have a much larger effect on frequency. Additionally, strict EM modelling approaches have some limitations at both low and high MWPD and are generally useful for identifying possible regions for the plasma to spark, but do not necessarily describe the plasma shape. Fully coupled EM/plasma models offer a better description which models the power and pressure size and electron density. Using multi-physics coupling of EM, plasma and heat transfer solutions, the spatial variation in diamond growth can be estimated.

CRediT authorship contribution statement

- Jerome A. Cuenca
  Conceptualization, Methodology, Software, Validation, Formal Analysis, Investigation, Writing - Original Draft, Writing – Review & Editing, Visualisation.
- Soumen Mandal
  Investigation, Resources, Supervision, Writing – Review & Editing
- Evan L. H. Thomas
  Investigation, Resources, Writing – Review & Editing
- Oliver A. Williams
  Resources, Supervision, Project Administration, Funding Acquisition.

Declaration of competing interest

The authors declare that they have no known competing financial interests or personal relationships that could have appeared to influence the work reported in this paper.

Acknowledgements

This project has been supported by Engineering and Physical Sciences Research Council (EPSRC) under the GaN-DaME program grant (EP/P00945X/1) and the European Research Council (ERC) Consolidator Grant under the SUPERNEMS Project (647471). SEM was carried out in the cleanroom of the ERDF-funded Institute for Compound Semiconductors (ICS) at Cardiff University. Experimental data to support this publication can be found at: http://doi.org/10.17035/d.2022.0155240777.

References

[1] R. Sachan, A. Bhaumik, P. Pant, J. Prater, J. Narayan, Diamond film growth by HFCVD on Q-carbon seeded substrate, Carbon 141 (2019) 182–189, https://doi.org/10.1016/j.carbon.2018.09.058.
[2] J. Narayan, A. Bhaumik, S. Gupta, P. Joshi, P. Riley, R. Narayan, Role of Q-carbon in nucleation and formation of continuous diamond film, Carbon 176 (2021) 558–568, https://doi.org/10.1016/j.carbon.2021.02.049.
[3] M. Amaral, A. Fernandes, M. Vila, F. Oliveira, R. Silva, Growth rate improvements in the hot-filament CVD deposition of nanocrystalline diamond, Diam. Relat. Mater. 15 (11–12) (2006) 1822–1827, https://doi.org/10.1016/j.diamond.2006.07.024.
[4] M. Ali, M. Ürgen, Surface morphology, growth rate and quality of diamond films synthesized in hot filament CVD system under various methane concentrations, Appl. Surf. Sci. 257 (20) (2011) 8420–8426, https://doi.org/10.1016/j.apsusc.2011.04.097.
[5] G.D. Barber, W.A. Yarbrough, Growth rate of diamond on polycrystalline ⟨110⟩ diamond substrates from carbon disulfide in hydrogen by hot-filament-assisted chemical vapor deposition, J. Am. Ceram. Soc. 80 (6) (1997) 1560–1566, https://doi.org/10.1111/j.1151-2916.1997.tb03016.x.
[6] T. Tabakoya, S. Kanada, Y. Wakui, Y. Takamori, T. Yamada, M. Nagai, et al., High-rate growth of single-crystalline diamond (100) films by hot-filament chemical vapor deposition with tantalum filaments at 3000 Å°C, Physica Status Solidi (A) Applications and Materials Science 216 (21) (2019) 4–7, https://doi.org/10.1002/pssa.201900244.
[7] X. Liang, L. Wang, H. Zhu, D. Yang, Effect of pressure on nanocrystalline diamond films deposition by hot filament CVD technique from CH4/H2 gas mixture, Surf. Coat. Technol. 202 (2) (2007) 261–267, https://doi.org/10.1016/j.surfcoat.2007.05.032.
[8] S. Mandal, K. Arts, H.C. Knoops, J.A. Cuenca, G.M. Klemencic, O.A. Williams, Surface zeta potential and diamond growth on gallium oxide single crystal, Carbon 181 (2021) 79–86, https://doi.org/10.1016/j.carbon.2021.04.100.
[9] A. Tallaire, O. Brinza, P. Huillery, T. Delord, C. Pellet-Mary, R. Staacke, et al., High NV density in a pink CVD diamond grown with N2O addition, Carbon 170 (2020) 421–429, https://doi.org/10.1016/j.carbon.2020.08.048.
[10] J. Weng, F. Liu, L.W. Xiong, J.H. Wang, Q. Sun, Deposition of large area uniform diamond films by microwave plasma CVD, Vacuum 147 (2018) 134–142, https://doi.org/10.1016/j.vacuum.2017.10.026.
[11] J.A. Cuenca, M.D. Smith, D.E. Field, F.C.-P. Massabuau, S. Mandal, J. Pomeroy, et al., Thermal stress modelling of diamond on GaN/III-nitride membranes, Carbon 174 (2021) 647–661, https://doi.org/10.1016/j.carbon.2020.11.067.
[12] P. Achatz, J.A. Garrido, M. Stutzmann, O.A. Williams, D.M. Gruen, A. Kromka, et al., Optical properties of nanocrystalline diamond thin films, Appl. Phys. Lett. 88 (10) (2006) 11–13, https://doi.org/10.1063/1.2183366.
[13] F. Bénédic, M. Belmahi, T. Easwarakhanthan, P. Alnot, In situ optical characterization during MPACVD diamond film growth on silicon substrates using a bichromatic infrared pyrometer under oblique incidence, J. Phys. D. Appl. Phys. 34 (7) (2001) 1048–1058, https://doi.org/10.1088/0022-3727/34/7/305.
[14] V.S. Sedov, A.K. Martyanov, A.A. Khomich, S.S. Savin, V.V. Voronov, R. A. Khmelnitskiy, et al., Co-deposition of diamond and β-SiC by microwave plasma CVD in H2-CH4-SiH4 gas mixtures, Diam. Relat. Mater. 98 (July) (2019), 107520, https://doi.org/10.1016/j.diamond.2019.107520.
[15] F. Fendrych, A. Taylor, L. Peksa, I. Kratochvilova, J. Vlcek, V. Rezacova, et al., Growth and characterization of nanodiamond layers prepared using the plasma-enhanced linear antennas microwave CVD system, J. Phys. D. Appl. Phys. 43 (37) (2010), https://doi.org/10.1088/0022-3727/43/37/374018.
[16] S. Ohmagari, H. Yamada, N. Tsubouchi, H. Umezawa, A. Chayahara, S. Tanaka, et al., Large reduction of threading dislocations in diamond by hot-filament chemical vapor deposition accompanying W incorporations, Appl. Phys. Lett. 113 (3) (2018), https://doi.org/10.1063/1.5040658.
[17] P. Mehta Menon, A. Edwards, C.S. Feigerle, R.W. Shaw, D.W. Coffey, L. Heatherly, et al., Filament metal contamination and Raman spectra of hot filament chemical vapor deposited diamond films, Diam. Relat. Mater. 8 (1) (1999) 101–109, https://doi.org/10.1016/S0925-9635(98)00444-0.
[18] S. Okoli, R. Haubner, B. Lux, Influence of the filament material on low-pressure hot-filament cvd diamond deposition, Le Journal de Physique IV 02 (C2) (1991) C2–923–C2–930. doi:https://doi.org/10.1051/jp4:19912111.
[19] A.P. Bolshakov, V.G. Ralchenko, V.Y. Yurov, A.F. Popovich, I.A. Antonova, A. A. Khomich, et al., High-rate growth of single crystal diamond in microwave plasma in CH4/H2 and CH4/H2/Ar gas mixtures in presence of intensive soot formation, Diam. Relat. Mater. 62 (2016) 49–57, https://doi.org/10.1016/j.diamond.2015.12.001.
[20] J. Achard, V. Jacques, A. Tallaire, Chemical vapour deposition diamond single crystals with nitrogen-vacancy centres: a review of material synthesis and technology for quantum sensing applications, J. Phys. D. Appl. Phys. 53 (31) (2020), https://doi.org/10.1088/1361-6463/ab81d1.

[21] A. Mallik, Microwave plasma CVD grown single crystal diamonds – a review, J. Coat. Sci. Technol. 3 (2) (2016) 75–99, https://doi.org/10.6000/2369-3355.2016.03.02.4.

[22] S. Nad, J. Asmussen, Analyses of single crystal diamond substrates grown in a pocket substrate holder via MPACVD, Diam. Relat. Mater. 66 (2016) 36–46, https://doi.org/10.1016/j.diamond.2016.03.007.

[23] G. Wu, M.H. Chen, J. Liao, The influence of recess depth and crystallographic orientation of seed sides on homoepitaxial growth of CVD single crystal diamonds, Diam. Relat. Mater. 65 (2016) 144–151, https://doi.org/10.1016/j.diamond.2016.03.011.

[24] A. Charris, S. Nad, J. Asmussen, Exploring constant substrate temperature and constant high pressure SCD growth using variable pocket holder depths, Diam. Relat. Mater. 76 (March) (2017) 58–67, https://doi.org/10.1016/j.diamond.2017.04.010.

[25] M. Füner, C. Wild, P. Koidl, Simulation and development of optimized microwave plasma reactors for diamond deposition, Surf. Coat. Technol. 116-119 (1999) 853–862, https://doi.org/10.1016/S0257-8972(99)00233-9.

[26] A.M. Gorbachev, V.A. Koldanov, A.L. Vikharev, Numerical modeling of a microwave plasma CVD reactor, Diam. Relat. Mater. 10 (3–7) (2001) 342–346, https://doi.org/10.1016/S0925-9635(00)00503-3.

[27] G. Shivkumar, S.S. Tholeti, M.A. Alrefae, T.S. Fisher, A.A. Alexeenko, Analysis of hydrogen plasma in a microwave plasma chemical vapor deposition reactor, J. Appl. Phys. 119 (11) (2016), https://doi.org/10.1063/1.4943025.

[28] F. Silva, X. Bonnin, J. Scharpf, A. Pasquarelli, Microwave analysis of PACVD diamond deposition reactor based on electromagnetic modelling, Diam. Relat. Mater. 19 (5–6) (2010) 397–403, https://doi.org/10.1016/j.diamond.2009.10.032.

[29] H. Yamada, A. Chayahara, Y. Mokuno, Y. Horino, S. Shikata, Simulation of temperature and gas flow distributions in region close to a diamond substrate with finite thickness, Diam. Relat. Mater. 15 (10) (2006) 1738–1742, https://doi.org/10.1016/j.diamond.2006.03.001.

[30] H. Yamada, Numerical simulations to study growth of single-crystal diamond by using microwave plasma chemical vapor deposition with reactive (H, C, N) species, Jpn. J. Appl. Phys. 51 (9) (2012), https://doi.org/10.1143/JJAP.51.090105.

[31] H. Yamada, A. Meier, F. Mazzocchi, S. Schreck, T. Scherer, Dielectric properties of single crystalline diamond wafers with large area at microwave wavelengths, Diam. Relat. Mater. 58 (2015) 1–4, https://doi.org/10.1016/j.diamond.2015.05.004.

[32] Y.F. Li, J.J. Su, Y.Q. Liu, M.H. Ding, X.L. Li, G. Wang, et al., Design of a new TM021 mode cavity type MPCVD reactor for diamond film deposition, Diam. Relat. Mater. 44 (2014) 88–94, https://doi.org/10.1016/j.diamond.2014.02.010.

[33] V.S. Sedov, A.K. Martyanov, A.A. Khomich, S.S. Savin, E.V. Zavedeev, V. G. Ralchenko, Deposition of diamond films on Si by microwave plasma CVD in varied CH4-H2 mixtures: reverse nanocrystalline-to-microcrystalline structure transition at very high methane concentrations, Diam. Relat. Mater. 109 (September) (2020), 108072, https://doi.org/10.1016/j.diamond.2020.108072.

[34] J. Su, Y. Li, M. Ding, X. Li, Y. Liu, G. Wang, et al., A dome-shaped cavity type microwave plasma chemical vapor deposition reactor for diamond films deposition, Vacuum 107 (2014) 51–55, https://doi.org/10.1016/j.vacuum.2014.04.002.

[35] X. Li, W. Tang, F. Wang, C. Li, L. Hei, F. Lu, A compact ellipsoidal cavity type microwave plasma reactor for diamond film deposition, Diam. Relat. Mater. 20 (3) (2011) 374–379, https://doi.org/10.1016/j.diamond.2011.01.025.

[36] P. Li, Z. Mao, Z. Peng, L. Zhou, Y. Chen, P.-H. Huang, et al., Acoustic separation of circulating tumor cells, Proc. Natl. Acad. Sci. U. S. A. 112 (16) (2015) 4970–4975, https://doi.org/10.1073/pnas.1504484112.

[37] F. Silva, K. Hassouni, X. Bonnin, A. Gicquel, Microwave engineering of plasma-assisted CVD reactors for diamond deposition, J. Phys. Condens. Matter 21 (36) (2009), 364202, https://doi.org/10.1088/0953-8984/21/36/364202.

[38] V. Sedov, A. Martyanov, A. Altakhov, A. Popovich, M. Shevchenko, S. Savin, et al., Effect of substrate holder design on stress and uniformity of large-area polycrystalline diamond films grown by microwave plasma-assisted cvd, Coatings 10 (10) (2020) 1–10, https://doi.org/10.3390/coatings10100939.

[39] J.-S. Yoon, M.-Y. Song, J.-M. Han, S.H. Hwang, W.-S. Chang, B. Lee, et al., Cross sections for Electron collisions with hydrogen molecules, J. Phys. Chem. Ref. Data 37 (2) (2008) 913–931, https://doi.org/10.1063/1.2838023.

[40] J.A. Cuenca, D.R. Slocombe, A. Porch, Temperature correction for cylindrical cavity perturbation measurements, IEEE Transactions on Microwave Theory and Techniques 65 (6) (2017) 2153–2161, https://doi.org/10.1109/TMTT.2017.2652462.

[41] J.A. Cuenca, D. Slocombe, A. Porch, Corrections to "temperature correction for cylindrical cavity perturbation measurements", IEEE Trans. Microwave Theory Tech. (2017) https://doi.org/10.1109/TMTT.2017.2751550.

[42] M. Füner, C. Wild, P. Koidl, Numerical simulations of microwave plasma reactors for diamond CVD, Surf. Coat. Technol. 74-75 (1995) 221–226, https://doi.org/10.1016/0257-8972(95)08232-8.

[43] H. Yamada, A. Chayahara, Y. Mokuno, S.I. Shikata, Model of reactive microwave plasma discharge for growth of single-crystal diamond, Jpn. J. Appl. Phys. 50 (1 PART 2) (2011), https://doi.org/10.1143/JJAP.50.01AB02.

[44] H. Yamada, A. Chayahara, Y. Mokuno, Simplified description of microwave plasma discharge for chemical vapor deposition of diamond, J. Appl. Phys. 101 (6) (2007), https://doi.org/10.1063/1.2711811.

[45] K. Hassouni, T.A. Grotjohn, A. Gicquel, Self-consistent microwave field and plasma discharge simulations for a moderate pressure hydrogen discharge reactor, J. Appl. Phys. 86 (1) (1999) 134–151, https://doi.org/10.1063/1.370710.

[46] I. Méndez, F.J. Gordillo-Vázquez, V.J. Herrero, I. Tanarro, Atom and ion chemistry in low pressure hydrogen DC plasmas, J. Phys. Chem. A 110 (18) (2006) 6060–6066, https://doi.org/10.1021/jp057182+.

[47] J.A. Cuenca, K.J. Sankaran, P. Pobedinskas, K. Panda, I.-N. Lin, A. Porch, et al., Microwave cavity perturbation of nitrogen doped nano-crystalline diamond films, Carbon 145 (2019) 740–750, https://doi.org/10.1016/j.carbon.2018.12.025.

[48] O.A. Williams, O. Douhéret, M. Daenen, K. Haenen, E. Osawa, M. Takahashi, Enhanced diamond nucleation on monodispersed nanocrystalline diamond, Chem. Phys. Lett. 445 (4–6) (2007) 255–258, https://doi.org/10.1016/j.cplett.2007.07.091.

[49] K.J. Sankaran, C.-J. Yeh, S. Kunuku, J.P. Thomas, P. Pobedinskas, S. Drijkoningen, et al., Microstructural effect on the enhancement of Field Electron emission properties of Nanocrystalline diamond films by Li-ion implantation and annealing processes, ACS Omega 3 (8) (2018) 9956–9965, https://doi.org/10.1021/acsomega.8b01104.

[50] A.F. Carvalho, T. Holz, N.F. Santos, M.C. Ferro, M.A. Martins, A.J. Fernandes, et al., Simultaneous CVD synthesis of graphene-diamond hybrid films, Carbon 98 (2016) 99–105, https://doi.org/10.1016/j.carbon.2015.10.095.

[51] M.W. Kelly, J.C. Richley, C.M. Western, M.N. Ashfold, Y.A. Mankelevich, Exploring the plasma chemistry in microwave chemical vapor deposition of diamond from C/H/O gas mixtures, J. Phys. Chem. A 116 (38) (2012) 9431–9446, https://doi.org/10.1021/jp306190n.

[52] N. Derkaoui, C. Rond, T. Gries, G. Henrion, A. Gicquel, Determining electron temperature and electron density in moderate pressure H2/CH4 microwave plasma, J. Phys. D. Appl. Phys. 47 (20) (2014), https://doi.org/10.1088/0022-3727/47/20/205201.

[53] O. A. Williams, Nanocrystalline diamond, Diamond and Related Materials 20 (5–6) (2011) 621–640. arXiv:0704.0701, doi:https://doi.org/10.1016/j.diamond.2011.02.015.

[54] S. Mandal, Nucleation of diamond films on heterogeneous substrates: a review, RSC Adv. 11 (17) (2021) 10159–10182, https://doi.org/10.1039/d1ra00397f.

[55] K.W. Hemawan, R.J. Hemley, Optical emission diagnostics of plasmas in chemical vapor deposition of single-crystal diamond, J. Vac. Sci. Technol. A 33 (6) (2015), 061302, https://doi.org/10.1116/1.4928031.

[56] S. Prawer, R. J. Nemanich, Raman spectroscopy of diamond and doped diamond., Philosophical transactions. Series A, Mathematical, physical, and engineering sciences 362 (1824) (2004) 2537–2565. doi:https://doi.org/10.1098/rsta.2004.1451.

[57] C. Ramaswamy, Raman effect in diamond, Nature 125 (3158) (1930) 704, https://doi.org/10.1038/125704b0.

[58] S. Bhagavantam, Relation of Raman effect to crystal structure, Indian J. Phys. 5 (1930) 169.

[59] D.S. Knight, W.B. White, Characterization of diamond films by Raman spectroscopy, J. Mater. Res. 4 (2) (1989) 385–393, https://doi.org/10.1557/JMR.1989.0385.

[60] Z.J. Ayres, J.C. Newland, M.E. Newton, S. Mandal, O.A. Williams, J. V. Macpherson, Impact of chemical vapour deposition plasma inhomogeneity on the spatial variation of sp^2 carbon in boron doped diamond electrodes, Carbon 121 (2017) 434–442, https://doi.org/10.1016/j.carbon.2017.06.008.

[61] K.J. Sankaran, J. Kurian, H.C. Chen, C.L. Dong, C.Y. Lee, N.H. Tai, et al., Origin of a needle-like granular structure for ultrananocrystalline diamond films grown in a N2/CH4plasma, J. Phys. D. Appl. Phys. 45 (36) (2012), https://doi.org/10.1088/0022-3727/45/36/365303.

[62] A.C. Ferrari, J. Robertson, Interpretation of Raman spectra of disordered and amorphous carbon, Phys. Rev. B 61 (20) (2000) 14095–14107, https://doi.org/10.1103/PhysRevB.61.14095.

[63] M.N. Ashfold, P.W. May, J.R. Petherbridge, K.N. Rosser, J.A. Smith, Y. A. Mankelevich, et al., Unravelling aspects of the gas phase chemistry involved in diamond chemical vapour deposition, Phys. Chem. Chem. Phys. 3 (17) (2001) 3471–3485, https://doi.org/10.1039/b104265n.

[64] Y.A. Mankelevich, M.N. Ashfold, J. Ma, Plasma-chemical processes in microwave plasma-enhanced chemical vapor deposition reactors operating with C/H/Ar gas mixtures, J. Appl. Phys. 104 (11) (2008), https://doi.org/10.1063/1.3035850.

[65] J.P. Gore, E.J. Mahoney, J.A. Smith, M.N. Ashfold, Y.A. Mankelevich, Imaging and modeling C2Radical emissions from microwave plasma-activated methane/hydrogen gas mixtures: contributions from chemiluminescent reactions and investigations of higher-pressure effects and plasma constriction, J. Phys. Chem. A 125 (19) (2021) 4184–4199, https://doi.org/10.1021/acs.jpca.1c01924.

[66] H. Yamada, A. Chayahara, Y. Mokuno, S. Shikata, Numerical microwave plasma discharge study for the growth of large single-crystal diamond, Diam. Relat. Mater. 54 (2015) 9–14, https://doi.org/10.1016/j.diamond.2014.11.005.